PAPER

Check for updates

Hydroxyl-oxygen vacancy synergy over In_2O_3–ZrO_2 catalysts: mechanistic insights into CO_2 hydrogenation to methanol†

Xia Li,‡[a] Zixia Feng,‡[b] Hanjun Lu,[a] Xinlin Hong, *[a] Guangchao Li *[bcde] and Shik Chi Edman Tsang[b]

The synergistic interplay between oxygen vacancies (O_V) and hydroxyl species in In_2O_3–ZrO_2 catalysts plays a crucial role in steering CO_2 hydrogenation pathways, however, the atomic-scale interactions between these features have remained elusive. In this study, we engineered In_2O_3–ZrO_2 solid solutions *via* ZrO_2 aerogel phase modulation and thoroughly elucidated the surface chemistry using advanced experimental techniques, including solid-state NMR, *in situ* DRIFTS, and adsorption studies. The results demonstrate that three distinct hydroxyl site types on the catalyst's surface (terminal hydroxyls (μ_1-OH), bridged hydroxyls (μ_2-OH), and triply bridging hydroxyls (μ_3-OH)) are in close spatial proximity. Besides, μ_2-OH and μ_3-OH are particularly susceptible to dihydroxylation, a process that facilitates the generation of O_V that serve as anchoring sites for CO_2. These hydroxyl-vacancy ensembles effectively promote CO_2 activation to carbonate/bicarbonate species, which then undergo selective hydrogenation to methanol *via* a formate-mediated pathway, thus establishing a self-sustaining catalytic cycle. This work clarifies the cooperative role of vacancy coordination and hydroxyl chemistry in CO_2 activation and provides a mechanistic guide for the rational design of bimetallic oxide catalysts for CO_2 hydrogenation to methanol.

1 Introduction

Dr Guangchao Li obtained his PhD in physical chemistry in 2021 at the University of Chinese Academy of Sciences (UCAS). He was a visiting PhD student at the University of Oxford (2019–2021). Later, he worked as a postdoctoral researcher at the Hong Kong Polytechnic University (PolyU). Since 2023, he has worked as a research assistant professor in the Department of Applied Biology and Chemical Technology at PolyU. His current research interests focus on the characterization and application of porous materials in energy conversion.

Guangchao Li

Since the inception of the "methanol economy" and "liquid sunshine", CO_2 hydrogenation to methanol has emerged as a pivotal technology for fossil fuel substitution strategies.[1–4] Bimetallic oxide catalysts, particularly those combining redox-active and structural-stabilizing components, have shown significant advantages in optimizing CO_2 activation kinetics and methanol selectivity. These benefits arise from their synergistic interfacial interactions and tailored electronic configurations.[5,6] However, the atomistic mechanisms driving these processes, particularly defect-mediated catalysis, remain poorly understood due to the inherent complexity of these systems. This complexity necessitates the use of model catalysts to understand underlying structure–activity relationships. This knowledge deficit motivates focused investigation of the In_2O_3–ZrO_2 system, where interfacial oxygen vacancies emerge as

[a]College of Chemistry and Molecular Sciences, Wuhan University, Wuhan 430072, China. E-mail: hongxl@whu.edu.cn

[b]Department of Applied Biology and Chemical Technology, The Hong Kong Polytechnic University, Hong Kong 999077, China. E-mail: guangchao.li@polyu.edu.hk

[c]The Hong Kong Polytechnic University Shenzhen Research Institute, The Hong Kong Polytechnic University, Shenzhen 518057, China

[d]PolyU-Daya Bay Technology and Innovation Research Institute, The Hong Kong Polytechnic University, Huizhou 516000, China

[e]Research Institute of Advanced Manufacturing (RIAM), Research Centre for Resources Engineering towards Carbon Neutrality (RCRE), The Hong Kong Polytechnic University, Hong Kong 999077, China

† Electronic supplementary information (ESI) available. See DOI: https://doi.org/10.1039/d5ta03275j

‡ These authors contributed to this paper equally.

catalytic linchpins linking macroscopic performance to atomic-scale phenomena.

Early studies on pure In_2O_3 revealed oxygen vacancies as critical for CO_2 activation, with the coordination environments governing product selectivity.[7] Triple-coordinated vacancies on specific crystal planes (*e.g.*, c-In_2O_3(111)) promote methanol formation *via* HCOO* stabilization, whereas double-coordinated vacancies favour CO production through C–O bond cleavage.[8] This reactivity highlights that vacancy geometry, not merely concentration, is the primary structural factor determining the selectivity of CO_2 hydrogenation pathways.[9] Since doping ZrO_2 brings additional complexity, there is an ongoing debate about the origin of the reactive oxygen vacancies.[10,11] Blum *et al.* attributed these vacancies to a partial reduction of In_2O_3 at the In_2O_3/m-ZrO_2 interface.[12] While Müller *et al.* demonstrated that the In-O_V-Zr structure, formed by the solvation of In^{3+} into the ZrO_2 lattice, serves as the true reactive centre.[13] Furthermore, Gong *et al.* reported that electron transfer modulates the electronic properties of the active sites, enhancing the selectivity toward methanol in ways that transcend the influence of vacancy concentration alone.[14] These findings challenge the simple vacancy-centred model, underscoring the multifaceted nature of catalytic selectivity in these systems.

Further investigations reveal that the surface chemical complexity of In_2O_3–ZrO_2 catalysts arises not only from the dynamic evolution of oxygen vacancies but also from the diversity of surface hydroxyl species.[15] Metal oxides inherently host a variety of hydroxyl groups, including terminal hydroxyls (μ_1-OH), doubly bridged hydroxyls (μ_2-OH), and triply bridged hydroxyls (μ_3-OH), whose stability and reactivity are governed by their local coordination environments.[16] Under thermal pretreatment and hydrogenation conditions, weakly bound hydroxyl groups are selectively destabilized *via* dehydration or heterolytic H_2 dissociation, thereby revealing distinct O_V configurations.[17] Moreover, the catalytic behaviour varies significantly among these hydroxyl groups. Previous studies have shown that the $In_{2O_3-x}(OH)_y$ surface is mainly composed of terminally bonded In–OH···In and bridged In–OH→In species, with only the former exhibiting the active frustrated Lewis pair (FLP) feature. This FLP efficiently dissociates H_2 and directs the selective conversion of CO_2 into CO.[18–20] This finding suggests that different hydroxyl-vacancy combinations exhibit conformational specificity in regulating the reaction pathways. Nevertheless, there is still a gap in the understanding of the mechanistic details within the more complex In_2O_3–ZrO_2 solid solution system.

In this work, we synthesized a series of composite supports containing monoclinic zirconia and tetragonal zirconia phases by heat treating ZrO_2 aerogel precursor. Subsequently, In_2O_3 was doped onto these supports to obtain In_2O_3–ZrO_2 catalysts featuring diverse hydroxyl sites. By employing magic-angle spinning solid-state nuclear magnetic resonance (MAS SSNMR), *in situ* diffuse reflectance infrared Fourier transform spectroscopy (DRIFTS), and chemical adsorption analysis techniques, we thoroughly investigated the surface chemical environment of the In_2O_3–ZrO_2 catalysts and elucidated the

synergistic interaction between hydroxyl groups and oxygen vacancies in the activation of CO_2 molecules. Our findings revealed that double and triple-coordinated O_V, especially those in the In–O_V–Zr configuration, serve as critical sites for CO_2 adsorption and activation. Moreover, hydroxyl groups adjacent to these asymmetric oxygen vacancies further stabilized CO_2 and facilitated subsequent hydrogenation processes. These insights provide an understanding of the reaction mechanism underlying CO_2 hydrogenation over bimetallic oxide catalysts.

2 Results and discussion

2.1 Catalytic performance for CO_2 hydrogenation

Mixed-crystal supports with varying proportions of m-ZrO_2 and t-ZrO_2 were prepared by calcining amorphous zirconia at 300, 400, 600, and 800 °C. Afterwards, four catalysts, designed as 10In400Zr300, 10In300Zr400, 10In300Zr600, and 10In300Zr800, were synthesized by wet impregnation with indium contents confirmed by ICP-OES (see full description in the Experimental section and Table S1, ESI†). It is noteworthy that the relative content of m-ZrO_2 in the catalyst increased with increasing calcination temperature of the supports (Table S1†). The CO_2 hydrogenation performance for these catalysts was evaluated over a temperature range of 250–310 °C at 5 MPa, enabling direct comparison with previous reports on In_2O_3–ZrO_2 catalysts. Prior to testing, all the catalysts were reduced at 350 °C in 10% H_2/Ar for 1 h unless otherwise noted. No methanol is formed from pure ZrO_2, and the space-time yield ($STY_{Methanol}$) of bare In_2O_3 is only 104.3 mg g_{cat}^{-1} h^{-1}, which is significantly lower than that of 10In300Zr400 (302 mg g_{cat}^{-1} h^{-1}) at 300 °C, 5 MPa, 12 000 mL g_{cat}^{-1} h^{-1} (Fig. S1 and Table S2†). Additionally, the In_2O_3–ZrO_2 catalyst synthesized *via* the one-step hydrothermal method performs worse than 10In300Zr400. This may be mostly In doped in ZrO_2, which is detrimental to methanol synthesis (Fig. S2 and S5†). Due to the competitive relationship between methanol synthesis and the reverse water-gas shift reaction, CO_2 conversion and methanol selectivity show a seesaw effect with increasing temperature (Fig. 1a).[21] Whereas, the process of increasing temperature promotes the activation of reactants and intermediates and exhibits higher $STY_{Methanol}$ (Fig. 1d). Moreover, the methanol yield is almost unchanged for up to 106 h, which is indicative of exceptional catalyst stability under prolonged reaction conditions (Fig. 1e).

Fig. 1b illustrates the variability in catalytic activity among the four catalysts examined at 290 °C. The results indicate that the catalyst labelled 10In300Zr800 exhibits almost no activity. In contrast, 10In300Zr400 shows superior catalytic performance at this temperature, achieving 83% methanol selectivity and 8% CO_2 conversion. Interestingly, as the m-ZrO_2 content in the support increases (Table S1†), the selectivity of the In_2O_3–ZrO_2 catalyst correspondingly improves. This enhancement in selectivity may be attributed to increased electron transfer between In_2O_3 and ZrO_2. To further investigate the relationship between methanol selectivity and m-ZrO_2 content, an identical mass fraction of indium was doped onto both m-ZrO_2 and t-ZrO_2 supports. Subsequently, the heterogeneous support prepared *via* the one-pot method was simulated by physical

This journal is © The Royal Society of Chemistry 2025

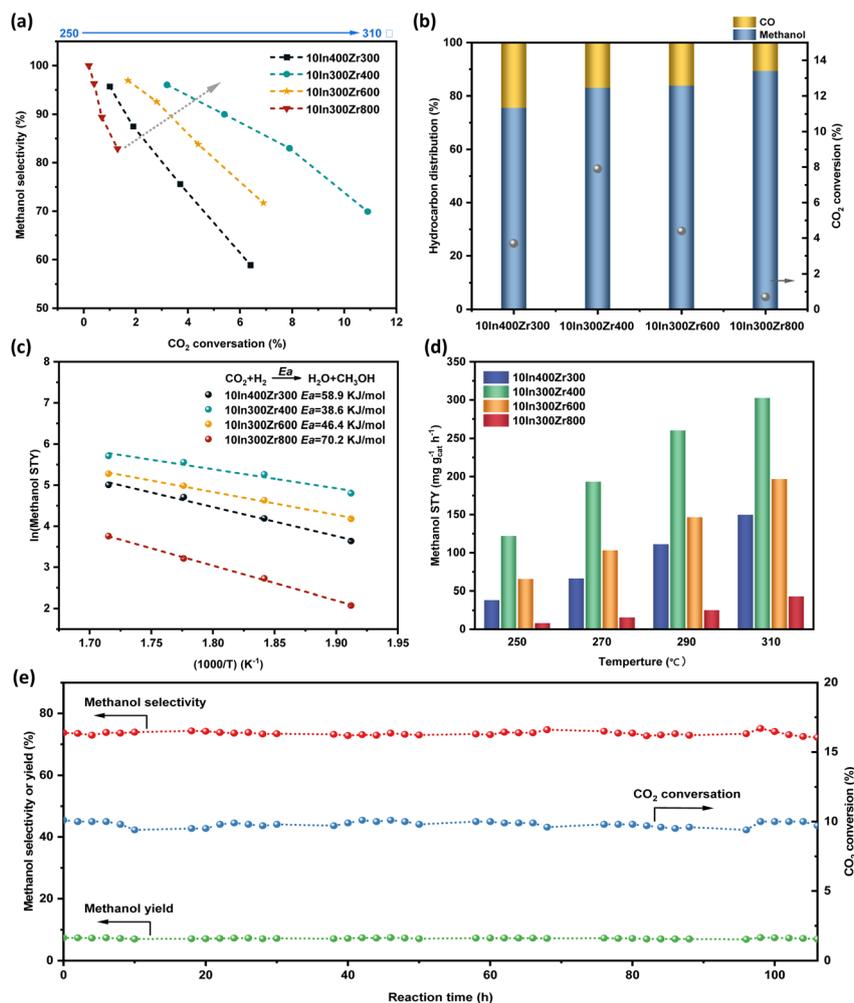*J. Mater. Chem. A*, 2025, **13**, 20542–20551 | **20543**

Fig. 1 Catalytic performance of 10In400Zr300, 10In300Zr400, 10In300Zr600, and 10In300Zr800 in the CO_2 hydrogenation reaction. (a) The correlation between methanol selectivity and CO_2 conversion at different reaction temperatures (for the same catalyst, each data point represents a temperature, 250, 270, 290 and 310 °C in that order), (b) CO_2 conversion and product distribution, (c) Arrhenius plots for the methanol synthesis reaction kinetics and the corresponding activation energy (E_a) calculations by using Arrhenius equation. (d) Relationship between the space-time yield (STY) of methanol and the reaction temperature. (e) Long-term TOS testing of 10In300Zr400. Reaction conditions: 0.1 g catalyst, GHSV = 12 000 mL g_{cat}^{-1} h^{-1}, 5 MPa, 310 °C, $H_2/CO_2 = 3$.

mixing to facilitate a comparative analysis (Fig. S2 and S3†). Testing under identical conditions confirmed that methanol selectivity positively correlates with the m-ZrO_2 content. Furthermore, the apparent activation energy (E_a) of the methanol synthesis reaction was calculated using the Arrhenius equation (Fig. 1c). The result indicates that the apparent activation energy of the 10In300Zr400 (38.6 kJ mol^{-1}) is noticeably lower than that of 10In400Zr300 (58.9 kJ mol^{-1}), 10In300Zr600 (46.4 kJ mol^{-1}), and 10In300Zr800 (70.2 kJ mol^{-1}), also showing a similar trend as CO_2 conversion. Thus, the above results indicate that 10In300Zr400 is most effective at lowering the energy barrier of the methanol synthesis and driving CO_2 into methanol.

2.2 Catalyst structure characterization

It is well known that the crystalline phase of ZrO_2 can undergo transformation in response to changes in the external environment, particularly temperature fluctuations, as evidenced by TG-DSC, XRD and Raman profiles (Fig. S4–S8†).[14,22] Previous studies have demonstrated that surface hydroxyl condensation drives the phase evolution of ZrO_2. The strong peak at 355 °C observed in the DSC curves is directly associated with the condensation of surface hydroxyls, which facilitates the transformation of a-ZrO_2 to t-ZrO_2.[23,24] In contrast, the weak peak at 481 °C corresponds to the phase change from t-ZrO_2 to m-ZrO_2.[25] Raman spectroscopy with 532 nm excitation was performed on four In_2O_3–ZrO_2 samples. As shown in Fig. S8,† the appearance of Raman peaks at 146 and 269 cm^{-1} correspond to the bulk of t-ZrO_2, whereas the m-ZrO_2 exhibits distinct Raman peaks at 178, 192, 333, and 378 cm^{-1}.[22] The 10In400Zr300 sample displays a dominant tetragonal phase. Notably, the intensity of the monoclinic phase (178 cm^{-1}) increases with higher calcination temperatures, reflecting a gradual phase transition from t-ZrO_2 to m-ZrO_2. These

20544 | *J. Mater. Chem. A*, 2025, **13**, 20542–20551

This journal is © The Royal Society of Chemistry 2025

spectral trends align with the XRD result, corroborating the structural evolution of the ZrO_2 support. Moreover, upon doping with 10 wt% In, the diffraction peaks corresponding to the (101) crystal plane (at ~30.2°, PDF#88-1007) of both fresh and spent 10In300Zr400 shift towards higher angles relative to those of Zr400. This shift indicates the incorporation of In into the ZrO_2 lattice, resulting in the formation of $InZrO_x$ solid solution (Fig. 2a).[13,26] Based on the Scherrer equation, the calculated particle sizes of 10In300Zr400 and 10In400Zr300 are in the range of 9–10 nm (Table S2†). The observed difference in catalytic activity between the two catalysts indicates that the crystal size has a relatively minor effect on the overall performance.

Although In_2O_3 diffraction signals are obscured due to peak overlap with t-ZrO_2, aberration-corrected HAADF-STEM images enable clear visualization of its distribution and structure. On 10In300Zr400 catalyst, In_2O_3 is well dispersed, likely facilitated by the abundant surface hydroxyl groups (Fig. 2b, c and S9†).[15,27] Images acquired at higher magnification of 10In300Zr400 reveal that the In atom is positioned at the top of the Zr atomic column in the form of brighter spots (Figure S10†). This observation aligns with the XRD results, confirming that some of the indium is embedded in zirconium oxide in the form of single atoms.[28,29] Moreover, the existence of indium single atoms is still observed on the spent catalysts, suggesting that this structure was extremely stable under high reaction temperatures.

Additionally, H_2-TPR measurements were performed to evaluate the H_2 dissociation behaviour, which further

elucidated the In_2O_3 morphology across the four In_2O_3–ZrO_2 catalysts (Fig. 2d and 5d). Compared with pure In_2O_3, the reduction peaks of the In_2O_3–ZrO_2 catalysts shift to higher temperatures, indicating a strong metal–support interaction (SMSI) between ZrO_2 and In_2O_3. This interaction promotes the partial reduction of In_2O_3, resulting in a more stable In–O–Zr structure and smaller In_2O_3 particles.[30] Also, the higher the proportion of m-ZrO_2 in the carrier, the lower the surface reduction temperature of In_2O_3. XPS analysis of the In 3d and Zr 3d spectra further supports these findings. Previous studies have shown that t-ZrO_2 and m-ZrO_2 have different electron transfer ability to In_2O_3, where the interfacial electron transfer from m-ZrO_2 to In–O–In is stronger.[14,31] In this study, we also observed that the binding energy of In exhibits a shift toward lower values, whereas the binding energy of Zr demonstrates a shift toward to higher values with increasing m-ZrO_2 content (Fig. 2e and f). This change suggests that the high electron density of In_2O_3 may contribute to the methanol selectivity. Moreover, although the H_2 dissociation ability of 10In300Zr400 is not the highest among the samples, its H_2 consumption is considerably greater than that of other systems, which promotes the formation of oxygen vacancies (Table S3†). These oxygen vacancies are essential for the effective activation and dissociation of H_2 and CO_2, as will be discussed in detail below.

2.3 Identification of surface hydroxyls and oxygen vacancies

The spatial configuration of the surface hydroxyls, which act as a key bridge between the catalyst crystal and the oxygen
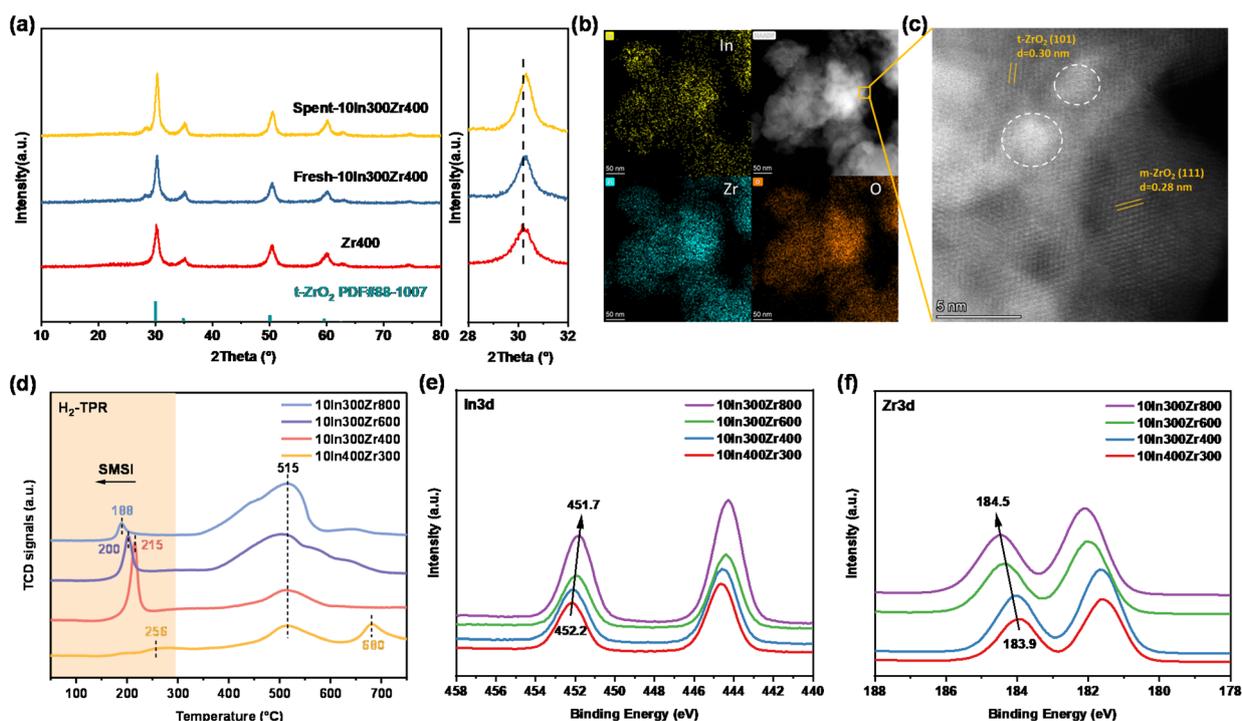

Fig. 2 Structural characterization and electronic effects. (a) XRD patterns of Zr400, fresh-10In300Zr400 and spent-10In300Zr400. (b) EDX elemental mapping and (c) HAADF-STEM images of fresh-10In300Zr400. (d) H_2-TPR profiles of the In_2O_3–ZrO_2 catalysts. XPS profiles of (e) In3d and (f) Zr3d for reduced 10In300Zr400.

vacancies, directly affects the exposure of the active sites. ^{1}H MAS SSNMR experiments were conducted to bring out the detailed structural information on the surface hydroxyls of In_2O_3, different crystalline ZrO_2, and the corresponding In_2O_3–ZrO_2 catalysts. As illustrated in Fig. 3a and S11,† In_2O_3, ZrO_2, and In_2O_3–ZrO_2 catalysts possess three types of surface hydroxyls. Within the range of 0–10 ppm, characteristic peaks of the surface hydroxyls emerge, with chemical shifts at 0–1.5 ppm, 1.6–3.8 ppm, and 3.9–5.0 ppm corresponding to the terminal hydroxyls (μ_1-OH), doubly bridged hydroxyls (μ_2-OH), and triply bridged hydroxyls (μ_3-OH), respectively (Fig. 3b).[16,32] The signals in the high-frequency regions (5.1–8.5 ppm) are attributed to the overlapping resonance of μ_2-OH and μ_3-OH, which contribute to the formation of extensive hydrogen-bonding networks. This spatial proximity is corroborated by the 2D [1]H–[1]H homonuclear correlation SSNMR spectra (Fig. 3c, S13–S15†), where strong diagonal peaks reveal the mutual interactions among μ_1-OH, μ_2-OH, and μ_3-OH. Additionally,

both In_2O_3 and ZrO_2 exhibit a μ_2-OH characteristic peak at 3.2 ppm, however, in the In_2O_3–ZrO_2 system, a new peak appears at 2.0 ppm. This observation suggests a significant alteration in the hydroxyl coordination environment, attributable to the formation of an In–O(H)–Zr heterointerface. Combining XRD and aberration-corrected HAADF-STEM results, it is inferred that the dissolution of In species onto the ZrO_2 surface leads to a partial reorganization of μ_3-OH groups. This reorganization results in the formation of an In–O(H)–Zr structure characterized by bimetallic coordination, directly contributing to a reduction in the μ_3-OH content in the composite catalyst and an increase in the ratio of μ_2-OH groups. These findings confirm the critical role of surface hydroxyls in stabilizing the active indium species and in determining their spatial distribution.

By analysing the ratio of various hydroxyl groups in ^{1}H MAS SSNMR and the total amount of acid sites obtained from NH_3-TPD measurements, we accurately calculated the specific
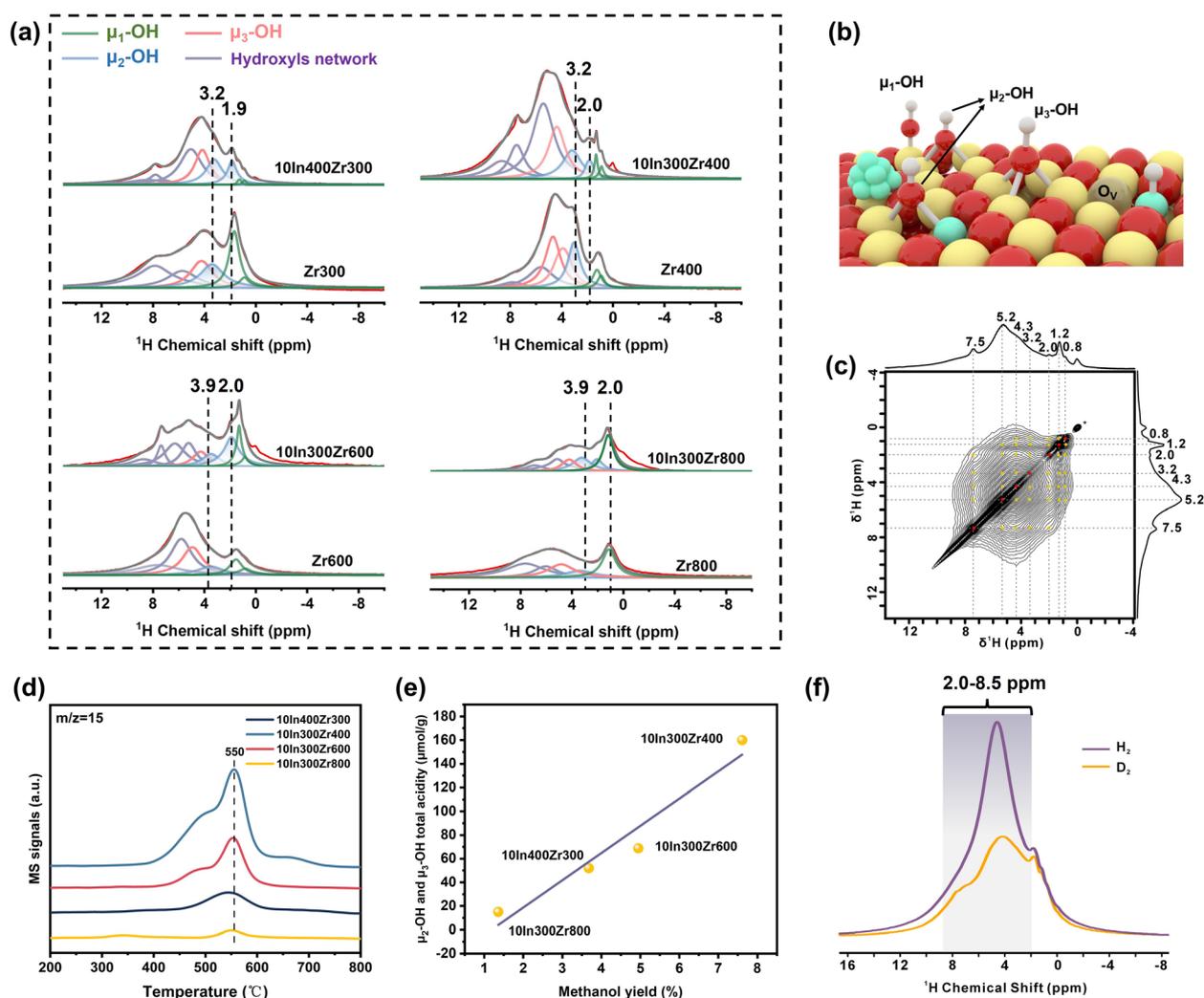

Fig. 3 Characterization of surface hydroxyl configurations and their structure–activity correlations. (a) ^{1}H MAS SSNMR spectra of In_2O_3–ZrO_2 catalysts and ZrO_2 supports, (b) schematic representation of the three types of surface hydroxyls, (c) 2D [1]H–[1]H homonuclear correlation SSNMR spectra of 10In300Zr400, (d) NH_3-TPD profiles of In_2O_3–ZrO_2 catalysts, (e) the proportion of μ_2-OH and μ_3-OH total acidity and methanol yield for CO_2 hydrogenation over In_2O_3–ZrO_2 catalysts, (f) ^{1}H MAS SSNMR spectra of H_2-D_2 exchange experiment for 10In300Zr400. Reaction condition: 0.1 g catalyst, GHSV = 12 000 mL g_{cat}^{-1} h^{-1}, 5 MPa, 310 °C, H_2/CO_2 = 3.

20546 | J. Mater. Chem. A, 2025, **13**, 20542–20551

This journal is © The Royal Society of Chemistry 2025

concentrations of different hydroxyl species in the catalysts. Upon analysing the NH_3-TPD profile through peak fitting (as detailed in Fig. 3d and Table S4†), a volcanic-like relationship emerges between the total acidity of the In_2O_3–ZrO_2 catalysts and their monoclinic phase content, with the catalyst labelled 10In300Zr400 possessing the highest concentration of acid sites (182 μmol g^{-1}). When correlating the total acidity of the catalysts with the methanol yield, a positive correlation trend akin to that between oxygen vacancy concentration and methanol yield is observed, which points to a link between oxygen vacancies and surface hydroxyls (Fig. S16†). Intriguingly, the total μ_2-OH and μ_3-OH concentrations of four In_2O_3–ZrO_2 catalysts show regular variations: 10In300Zr400 > 10In300Zr600 > 10In400Zr300 > 10In300Zr800, and this order coincides with a significant linear correlation with their methanol yield (Fig. 3e). Taking this into account, it is reasonable to speculate that μ_2-OH and μ_3-OH may be the active site for methanol synthesis. To confirm this point, we adsorbed H_2 on the catalyst surface and then switched D_2 to exchange the surface hydrogen species to obtain the ^1H SSNMR spectra (Fig. 3f). Our results show that a significant attenuation of both μ_2-OH and μ_3-OH signals in the 2.0–8.5 ppm region after D_2 treatment suggests that the two types of hydroxyl groups are highly reactive. In corroboration with this, O 1s XPS analysis shows a decrease in the hydroxyl group fraction after the reduction treatment and an increase in the oxygen vacancy fraction. Therefore, we propose that μ_2-OH and μ_3-OH are structural precursors of the active site, which may be generated by dehydroxylation to oxygen vacancies during the reaction process.

More information on the density of oxygen vacancies is unravelled in the O 1s spectra by XPS. As shown in Fig. 4a, the broad peak of the O 1s spectra can be deconvoluted into three different components. The peak at the lower binding energy (529.8 eV) is associated with the lattice oxygen of ZrO_2 (O_L). The two peaks centered at ca. 531.2 eV and 532.4 eV originate from O atoms in the proximity of an oxygen vacancy (O_V) and the chemisorbed oxygen species related to the surface hydroxyls (*OH). The radio of $O_V/(O_L + O_V + OH)$ and $OH/(O_L + O_V + OH)$ reflects the density of surface oxygen vacancies and the surface hydroxyls, respectively.[30,33] It is worth noting that doping In on Zr400 increases the concentration of O_V without changing *OH concentration, regarded as interfacial oxygen vacancies formed via the penetration of In into ZrO_2. Also, after reducing 10In300Zr400 by H_2, the oxygen vacancy concentration is increased from 21.4% to 26.9%, while the hydroxyl group concentration is decreased from 11.3% to 9.26% (Fig. S17†). Thus, some of the oxygen vacancies on the catalyst surface are derived from the oxidation of surface hydroxyls. Surface oxygen vacancies, as electron-rich centres, can effectively activate CO_2 molecules, and are usually regarded as important active sites for methanol synthesis by CO_2 hydrogenation. Systematic comparison of the composition–performance relationships among different catalyst systems revealed that O_V and OH concentrations in reduced catalysts follow the order
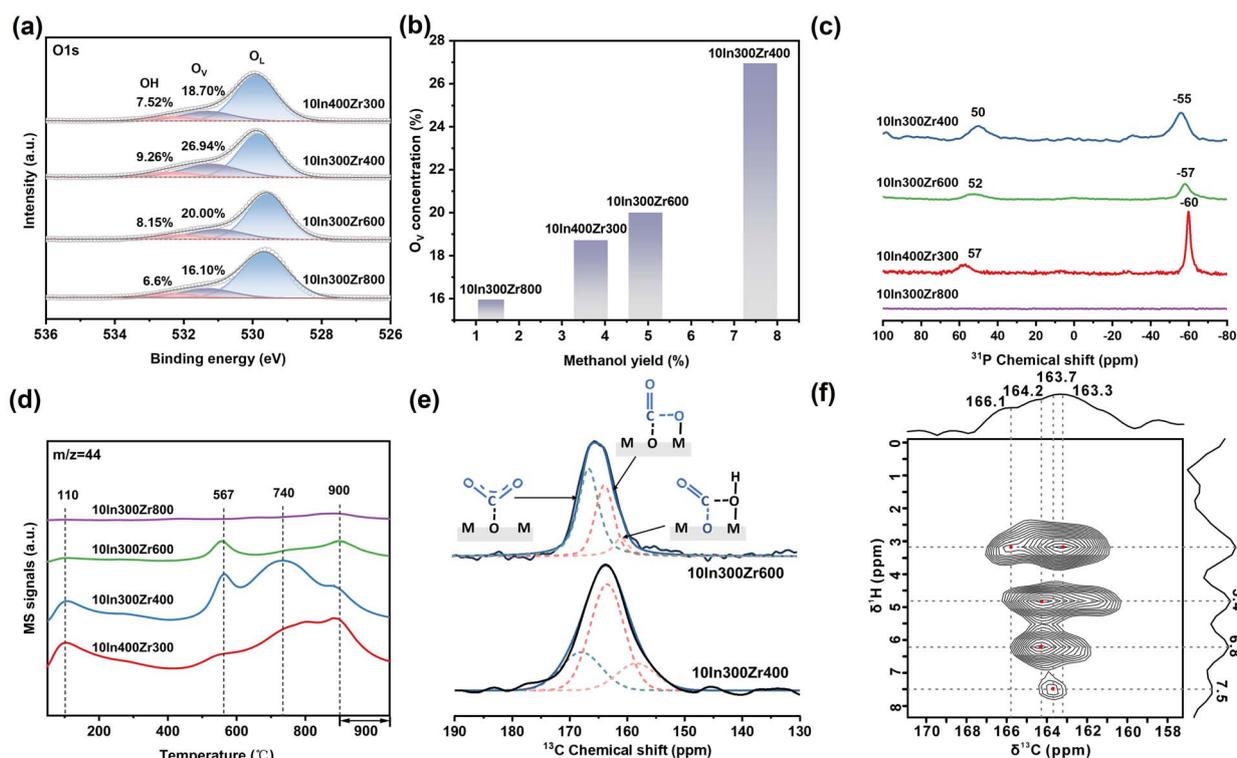

Fig. 4 Characterization for revealing the relationship between oxygen vacancies and CO_2 activation. (a) Deconvoluted O 1s XPS spectra In_2O_3–ZrO_2 catalysts, (b) the proportion of Ov concentration and methanol yield for CO_2 hydrogenation over In_2O_3–ZrO_2 catalysts, (c) ^{31}P MAS SSNMR spectra of TMP adsorbed on In_2O_3–ZrO_2 catalysts, (d) CO_2-TPD profiles of In_2O_3–ZrO_2 catalysts, (e) 1D ^{13}C MAS NMR spectra of CO_2 adsorbed on 10In300Zr400 and 10In300Zr600. (f) 2D ^{13}C–^1H heteronuclear correlation MAS SSNMR spectra of 10In300Zr400.

This journal is © The Royal Society of Chemistry 2025

J. Mater. Chem. A, 2025, **13**, 20542–20551 | **20547**

10In300Zr400 > 10In300Zr600 > 10In400Zr300 > 10In300Zr800, both exhibiting linear correlations with methanol synthesis activity (Fig. 4b and S18†). This result aligns with Liu et al.'s study,[15] where air plasma treatment enhanced the hydrophilicity of ZrO_2. In the highly hydrophilic 1% Ru/DBD-ZrO_2 catalyst, CO_2 is captured at oxygen vacancies, and the H atoms from surface OH* combine with CO_2 to form HCO_3* intermediates, which further convert to HCOO*. Although their work focused on CO_2 hydrogenation to CO, we propose that oxygen vacancies and hydroxyl groups serve as critical active sites and descriptors for catalyst structure–activity relationships, given the established role of formate as a key intermediate in methanol synthesis.

SSNMR is a powerful technique for the characterization of active sites on the solid materials.[34–36] As the TMP molecule is highly alkaline, TMP-assisted ^{31}P MAS SSNMR analysis was adopted to distinguish the acid sites over the catalysts.[37] Previous studies have shown that TMP is more sensitive to Lewis acidity than Brønsted acidity, and the signal ranging from −30 to −58 ppm is attributed to TMP binding onto the LAS.[38] Fig. 4c shows that for all catalysts except 10In300Zr800, two peaks are observed at −50 to −60 ppm and 40 to 60 ppm, respectively. The signals at −60, −57, and −55 ppm are assigned to Lewis acid sites in 10In400Zr300, 10In300Zr600, and 10In300Zr400, respectively. Apparently, 10In300Zr400 exhibits stronger Lewis acidity than both 10In300Zr600 and 10In400Zr300, which aligns with the increased oxygen vacancy concentration observed in the O 1s spectra. The signal in the positive chemical shift range corresponds to TMPO, formed by the reaction between TMP and lattice oxygen, indicating that the In_2O_3–ZrO_2 catalyst readily forms more oxygen vacancies.[39]

To investigate the effect of Lewis acidity/basicity of In_2O_3–ZrO_2 catalysts on the CO_2 adsorption and activation, the CO_2-TPD measurement was performed, as CO_2 molecules could bind strongly to FLP. The signals of CO_2 were collected by the mass spectrometer. As shown in Fig. 4d, CO_2 desorption peaks can be divided into three regions, 0–200 °C, 200–400 °C, and 400–900 °C, which are attributed to weak, medium-strong, and strong basic sites, respectively. In the temperature range below 400 °C, the two signals correspond to the physically adsorbed CO_2 and CO_2 adsorbed on the weakly basic site, like surface hydroxyls.[40,41] In the high temperature range of 400–900 °C, three consecutive desorption peaks at around 560, 740, and 900 °C are observed for all catalysts. These peaks are assigned to CO_2 adsorbed as bidentate carbonates (b-CO_3^{2-}) and monodentate carbonates (m-CO_3^{2-}) on the strongly basic sites (O_V).[42] Compared with the CO_2-TPD profiles of pure ZrO_2, we noticed that a larger peak area in the high temperature region for 10In300Zr400, which indicates that the oxygen vacancy concentration is elevated after doping with In, and this result is also evidenced by H_2-TPR and O 1s XPS (Fig. S19†). Analogously, the existence of more surface oxygen vacancies on 10In300Zr400 is further verified. To explore the effect of H_2 pretreatment on the surface properties of the catalysts, the In_2O_3–ZrO_2 catalysts were exposed to H_2 and Ar atmospheres at 350 °C for reduction and heat treatment, respectively (Fig. S20†). Obviously, after treatment with H_2, the signal intensities in the low-temperature region (<200 °C) decrease while the peak in the high-temperature region increases, suggesting that H_2 reduction creates more oxygen vacancies by removing the surface hydroxyls.

Meanwhile, high-resolution 1D ^{13}C MAS SSNMR and 2D ^{13}C–^1H Heteronuclear Correlation (HETCOR) MAS SSNMR spectra have been utilized to precisely elucidate the adsorption behaviour and structure of CO_2 over the catalyst surface. In general, the electron-rich oxygen atoms in the CO_2 molecule are anchored by Lewis acids (O_V) and are immobilized on the catalyst surface in the form of bidentate carbonates (b-CO_3^{2-}) and monodentate carbonates (m-CO_3^{2-}). As depicted in Fig. 4e, three ^{13}C signals are observed in the 158–175 ppm region after introducing $^{13}CO_2$ to In_2O_3–ZrO_2. The peaks from 158 to 162 ppm, 163 to 167 ppm, and 167 to 171 ppm correspond to bicarbonate, bidentate carbonate, and monodentate carbonate, respectively.[43] Furthermore, the 2D ^{13}C–^1H HETCOR MAS SSNMR experiments reveal the spatial proximity of the adsorbed $^{13}CO_2$ and the three surface hydroxyls (Fig. 4f and S21†). Apparently, the b-CO_3^{2-} species in the 163–167 ppm regime exhibits strong interactions with structural hydroxyl groups of μ_2-OH and μ_3-OH, as well as their associated hydrogen-bonding network. No correlation peak corresponding to an interaction with μ_1-OH is observed. Therefore, we conclude that μ_2-OH and μ_3-OH adjacent to O_V act synergistically as proton donors to promote CO_2 protonation to HCO_3^- on the one hand, and by stabilizing b-CO_3^{2-} through the O–H⋯O bond on the other, thereby providing an optimized microenvironment for CO_2 hydrogenation.

2.4 Investigation of the reaction mechanism

In situ DRIFTS measurements were conducted to elucidate the synergistic effect of surface hydroxyls and oxygen vacancies in methanol synthesis. Fig. 5a presents the real-time monitoring of the catalytic process over the 10In300Zr400 catalysts under programmed temperature conditions. When the test temperature is controlled at 100 °C, a broad absorption band in the range of 1660 and 1200 cm^{-1} is observed, which can be attributed to the formation of carbonate or bicarbonate species. Specifically, the peaks at 1276, 1300, 1662 cm^{-1} and 1508, 1335 cm^{-1} are assigned to bidentate carbonate species (b-CO_3^{2-}) and monodentate carbonate (m-CO_3^{2-}), respectively. In addition, peaks at 1446 and 1624 cm^{-1} correspond to bidentate bicarbonate species (b-HCO_3^-).[44] These findings suggest that CO_2 is predominantly adsorbed on the reduced catalyst as carbonates and bicarbonates, consistent with CO_2-TPD and ^{13}C MAS SSNMR results. Moreover, linearly adsorbed CO (2077 cm^{-1}) is also observed at 100 °C, which may originate from the dissociation of carbonates induced by surface oxygen vacancies, as supported by the literature.[42] As the temperature increases, the band of carbonate species and bicarbonate species gradually diminish, while new spectral features emerge. These new features correspond to the formation of bidentate formates (b-HCOO*, 1392, 1376, 1592 cm^{-1}) and methoxy (CH$_3$O*, 1046 and 1140 cm^{-1}).[45,46] Notably, upon reaching 250 °C, the HCOO* absorption peak intensity markedly increases, while the HCOO*/CH$_3$O* ratio initially rise but
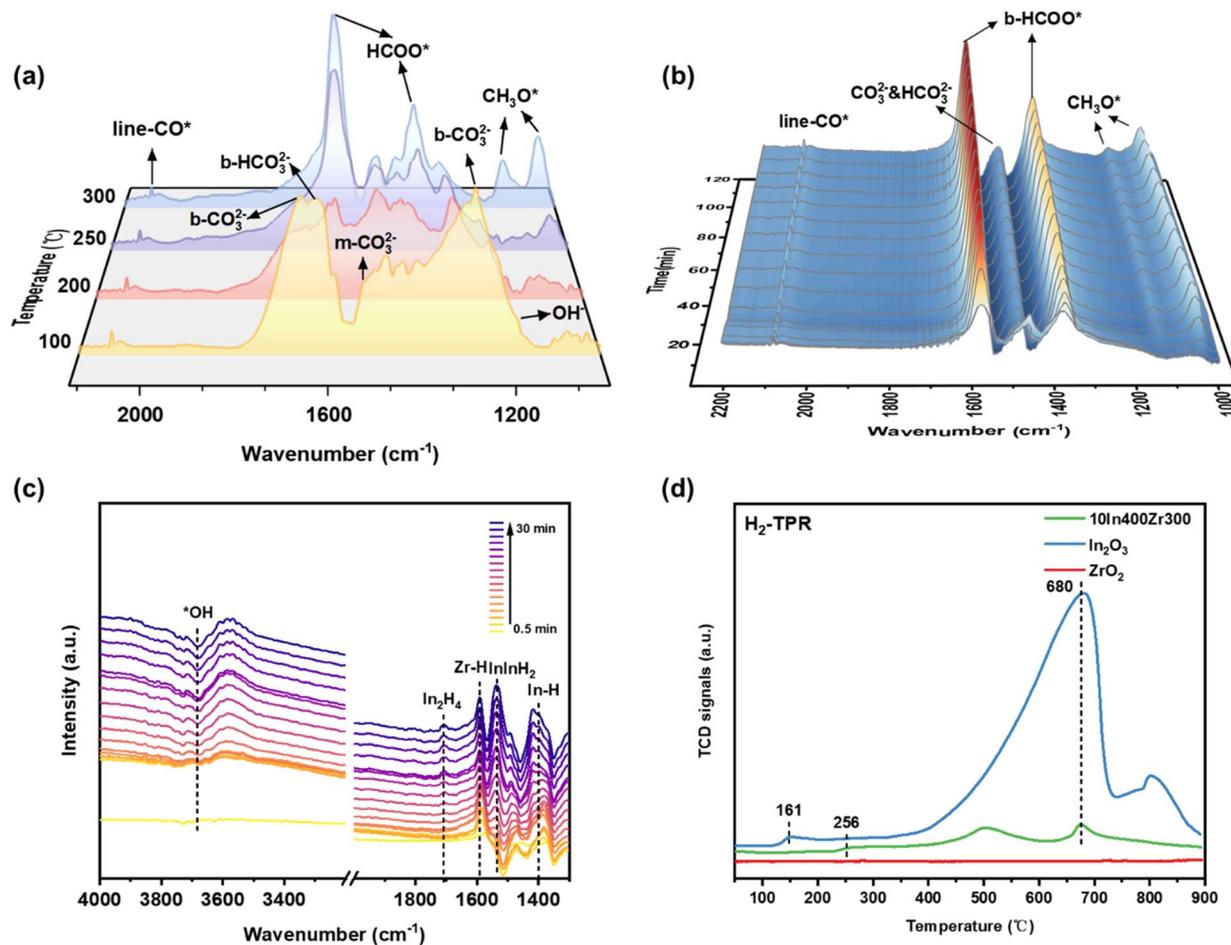
20548 | J. Mater. Chem. A, 2025, 13, 20542–20551

This journal is © The Royal Society of Chemistry 2025

Fig. 5 *In situ* DRIFTS spectra of $CO_2 + H_2$ reaction in the range of $1000-2200$ cm^{-1} over 10In300Zr400 catalyst. (a) DRIFTS spectra at different temperatures ($100-300$ °C) after reacting for 1 h, (b) time-resolved DRIFTS spectra at a reaction temperature of 300 °C; (c) DRIFTS spectra of H_2 reduction at 350 °C; (d) H_2-TPR profiles of ZrO_2, In_2O_3, 10In400Zr300.

subsequently decline, suggesting that HCOO* acts as a key intermediate in the CO_2 hydrogenation pathway, with its conversion to CH_3O* requiring a high activation energy barrier (Fig. S22†). Furthermore, time-resolved DRIFTS analysis at 300 °C captures the dynamic behaviour of reaction intermediates (Fig. 5b). Initially observed carbonate and bicarbonate species, analogous to those at 100 °C, show rapid intensity decay within 10 minutes, while HCOO* and CH_3O* species progressively increase, indicating the conversion of carbonate/bicarbonate to formate on the In_2O_3–ZrO_2 catalysts.

To further elucidate the hydrogen dissociation mechanism on the In_2O_3–ZrO_2 catalyst, we also conducted *in situ* DRIFTS experiments under hydrogen-rich conditions at 350 °C and 1 MPa. As illustrated in Fig. 5c, upon exposure to a hydrogen atmosphere, the characteristic peak corresponding to surface hydroxyls (OH*, 3684 cm^{-1}) on the 10In300Zr400 catalyst demonstrates a progressive intensity reduction. Meanwhile, distinct shifts at 1707, 1584, 1533, and 1390 cm^{-1} appear, which can be assigned to the intermediate In_2H_4, Zr–H, $InInH_2$, and InH species.[47] Previous studies have demonstrated that molecular hydrogen preferentially adsorbs on the In_2O_3 surface, where it readily undergoes heterolytic dissociation to form indium

hydride species.[19] This preferential adsorption behaviour is supported by both theoretical calculations and surface characterization techniques.[7,48] In contrast, H_2-TPR has revealed that ZrO_2 exhibits a strong tendency to interact with carbon-based species rather than hydrogen molecules, indicating its limited capability for hydrogen dissociation under similar conditions (Fig. 5d).[49,50] These collectively suggest that while hydrogen molecules remove surface hydroxyls, they simultaneously generate electron-rich InH species on the indium oxide surface. Accordingly, Zr–H species are likely formed through a hydrogen spillover mechanism from the adjacent In_2O_3 surface, rather than through direct dissociation on ZrO_2.[11] This hydrogen migration phenomenon is consistent with the well-documented surface mobility of hydrogen atoms in mixed oxide systems.

2.5 Discussion on hydroxyl-oxygen vacancy synergy

Based on the experimental results discussed above, Fig. 6 illustrates the proposed surface chemical environment of the In_2O_3–ZrO_2 catalyst and delineates the synergistic mechanism between hydroxyl groups and oxygen vacancies in the activation of CO_2 molecules. The crystalline phase of ZrO_2 is usually
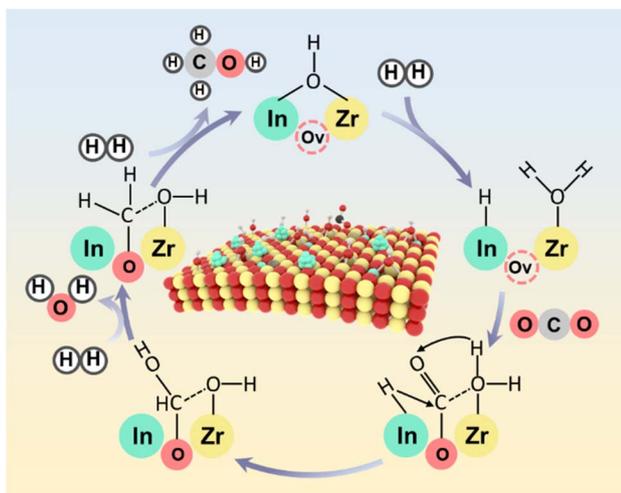
This journal is © The Royal Society of Chemistry 2025

J. Mater. Chem. A, 2025, **13**, 20542–20551 | **20549**

Fig. 6 Schematic representation of CO_2 hydrogenation to methanol over In_2O_3–ZrO_2 catalysts.

closely related to the distribution of surface hydroxyls. We found that 400 °C approaches the critical phase transition temperature of ZrO_2, and calcination at temperatures above this threshold enables the formation of mixed-crystalline supports. The 10In300Zr400 catalyst constructed on mixed-crystalline ZrO_2 by low-temperature calcination is enriched with a higher O_V concentration at the interface while simultaneously maintaining a greater density of surface hydroxyls. According to XPS and XRD results, the more severe lattice mismatch between the mixed-crystalline ZrO_2 and In_2O_3, which creates a greater number of interfacial oxygen vacancies than in pure t-ZrO_2.[28] Compared to the physical mixed system with the same mixed-crystal composition, the catalysts synthesised by the one-pot method exhibit higher CO_2 conversion than, confirming that *in situ* construction of interfacial oxygen vacancies is the key to the formation of active sites (Fig. S2†). The atomic-level dispersion of In_2O_3 is promoted through surface hydroxyls and strong metal–support interactions, thereby increasing the number of active sites. However, further elevation of calcination temperatures leads to particle coarsening and reduced hydroxyl group concentration, resulting in a reduction of hydroxyl-oxygen vacancy active sites and a decline in catalytic performance. During CO_2 hydrogenation, H_2 preferentially dissociates at In-containing structural sites, such as In nanoclusters and the In–O(H)–Zr structure. This process exposes oxygen vacancies that exist in double- and triple-bridged coordination environments. These oxygen vacancies function as strong Lewis acid sites, anchoring the oxygen atoms of CO_2, while the neighbouring μ_2-OH/μ_3-OH network forms FLP sites through hydrogen bonding. This synergistic interaction promotes the formation of carbonate and bicarbonate in a locally polar environment. The CO_2 species stabilized by the hydroxyl network are activated in the presence of the In–H active site, leading to directed hydrogenation to methanol *via* formate intermediate. Throughout the reaction, the depleted hydroxyl groups and oxygen vacancies are dynamically regenerated by

surface remodelling under reaction conditions, thereby creating a hydroxyl-oxygen vacancy synergistic catalytic cycle.

3 Conclusions

In summary, a straightforward In_2O_3–ZrO_2 model catalyst was utilized to investigate the distribution of surface hydroxyls and to elucidate the synergistic interactions and transformations between oxygen vacancies and surface hydroxyls in CO_2 hydrogenation to methanol. Among the catalysts tested-10In400Zr300, 10In300Zr400, 10In300Zr600, and 10In300Zr800 -the 10In300Zr400 catalyst exhibits a higher concentration of surface hydroxyls and oxygen vacancies. Under the operating conditions of 300 °C, 5 MPa, and 12 000 mL g_{cat}^{-1} h^{-1}, it achieved superior methanol synthesis activity (302 mg g_{cat}^{-1} h^{-1}). Structural characterization and mechanistic studies revealed that the FLP sites formed by surface hydroxyls and oxygen vacancies, act as centres for stabilizing CO_2, providing an abundant carbon source for the formation of methanol synthesis intermediates, HCOO* and CH_3O*. Overall, this work reinterprets the physicochemical behaviour of small molecule reactants on the catalyst surface from an acid–base perspective, offering novel insights for designing catalysts with high-density active interfacial sites for enhanced performance.

Data availability

The data supporting this article have been included as part of the ESI.†

Author contributions

Xia Li: data curation, software, formal analysis, writing–original draft, writing–review & editing. Zixia Feng: investigation, data curation, formal analysis, resources, methodology. Hanjun Lua: investigation, formal analysis. Xinlin Hong: writing– review & editing, guiding the project. Guangchao Li: writing– review & editing, guiding the project. Shik Chi Edman: discussion.

Conflicts of interest

There are no conflicts to declare.

Acknowledgements

Notes and references

1 G. A. Olah, *Angew. Chem., Int. Ed.*, 2005, **44**, 2636–2639.

20550 | *J. Mater. Chem. A*, 2025, **13**, 20542–20551

This journal is © The Royal Society of Chemistry 2025

2 C. F. Shih, T. Zhang, J. Li and C. Bai, *Joule*, 2018, **2**, 1925–1949.

3 P. Gao, L. Zhang, S. Li, Z. Zhou and Y. Sun, *ACS Cent. Sci.*, 2020, **6**, 1657–1670.

4 H. Wang, X. Liu, P. Niu, S. Wang, J. Shi and L. Li, *Matter*, 2020, **2**, 1377–1413.

5 F. Tao, *Chem. Soc. Rev.*, 2012, **41**, 7977–7979.

6 X. Jiang, X. Nie, X. Guo, C. Song and J. G. Chen, *Chem. Rev.*, 2020, **120**, 7984–8034.

7 J. Ye, C. Liu, D. Mei and Q. Ge, *ACS Catal.*, 2013, **3**, 1296–1306.

8 S. Dang, B. Qin, Y. Yang, H. Wang, J. Cai, Y. Han, S. Li, P. Gao and Y. Sun, *Sci. Adv.*, 2020, **6**, eaaz2060.

9 W. Wang, K. Huo, Y. Wang, J. Xie, X. Sun, Y. He, M. Li, J. Liang, X. Gao, G. Yang, S. Lin, F. Cao, H. Jiang, M. Wu and N. Tsubaki, *ACS Catal.*, 2024, **14**, 9887–9900.

10 N. H. M. D. Dostagir, C. R. Tomuschat, K. Oshiro, M. Gao, J.-y. Hasegawa, A. Fukuoka and A. Shrotri, *JACS Au*, 2024, **4**, 1048–1058.

11 F. Gao, Y. Wang, Y. Zhao, K. Wang, W. Guo, Z. Sun, Y. Zhu, H. He, Y. Liu and Y. Cao, *ACS Catal.*, 2025, **15**, 2785–2795.

12 X. Zhang, A. V. Kirilin, S. Rozeveld, J. H. Kang, G. Pollefeyt, D. F. Yancey, A. Chojecki, B. Vanchura and M. Blum, *ACS Catal.*, 2022, **12**, 3868–3880.

13 A. Tsoukalou, P. M. Abdala, A. Armutlulu, E. Willinger, A. Fedorov and C. R. Müller, *ACS Catal.*, 2020, **10**, 10060–10067.

14 C. Yang, C. Pei, R. Luo, S. Liu, Y. Wang, Z. Wang, Z.-J. Zhao and J. Gong, *J. Am. Chem. Soc.*, 2020, **142**, 19523–19531.

15 M. Liu, R. Zou and C.-J. Liu, *Appl. Catal., B*, 2025, **360**, 124549.

16 Q. Han, P. Gao, L. Liang, K. Chen, A. Dong, Z. Liu, X. Han, Q. Fu and G. Hou, *Anal. Chem.*, 2021, **93**, 16769–16778.

17 L. Fu, Z. Qu, L. Zhou and Y. Ding, *ACS Sustain. Chem. Eng.*, 2024, **12**, 18412–18421.

18 G. C. Welch, R. R. S. Juan, J. D. Masuda and D. W. Stephan, *Science*, 2006, **314**, 1124–1126.

19 K. K. Ghuman, L. B. Hoch, T. E. Wood, C. Mims, C. V. Singh and G. A. Ozin, *ACS Catal.*, 2016, **6**, 5764–5770.

20 R. Jing, X. Lu, J. Wang, J. Xiong, Y. Qiao, R. Zhang and Z. Yu, *Small*, 2024, **20**, 2310926.

21 S. Tada, S. Kayamori, T. Honma, H. Kamei, A. Nariyuki, K. Kon, T. Toyao, K.-i. Shimizu and S. Satokawa, *ACS Catal.*, 2018, **8**, 7809–7819.

22 M. Li, Z. Feng, P. Ying, Q. Xin and C. Li, *Phys. Chem. Chem. Phys.*, 2003, **5**, 5326–5332.

23 X. Guo, D. Mao, G. Lu, S. Wang and G. Wu, *Catal. Commun.*, 2011, **12**, 1095–1098.

24 Y. Wu, J. Chen, W. Hu, K. Zhao, P. Qu, P. Shen, M. Zhao, L. Zhong and Y. Chen, *J. Catal.*, 2019, **377**, 565–576.

25 Z. Yanwei, G. Fagherazzi and S. Polizzi, *J. Mater. Sci.*, 1995, **30**, 2153–2158.

26 T. Yan, N. Li, L. Wang, W. Ran, P. N. Duchesne, L. Wan, N. T. Nguyen, L. Wang, M. Xia and G. A. Ozin, *Nat. Commun.*, 2020, **11**, 6095.

27 H. Li, W. Wang, S. Xue, J. He, C. Liu, G. Gao, S. Di, S. Wang, J. Wang, Z. Yu and L. Li, *J. Am. Chem. Soc.*, 2024, **146**, 9124–9133.

28 M. S. Frei, C. Mondelli, A. Cesarini, F. Krumeich, R. Hauert, J. A. Stewart, D. Curulla Ferré and J. Pérez-Ramírez, *ACS Catal.*, 2019, **10**, 1133–1145.

29 H. Li, S. Di, P. Niu, S. Wang, J. Wang and L. Li, *Energy Environ. Sci.*, 2022, **15**, 1601–1610.

30 Y. Zhou, L. Liu, G. Li and C. Hu, *ACS Catal.*, 2021, **11**, 7099–7113.

31 C. Shen, K. Sun, R. Zou, Q. Wu, D. Mei and C. J. Liu, *Appl. Catal., B*, 2025, **361**, 124683.

32 J. Qin, J. Long, F. Sun, P. P. Zhou, W. D. Wang, N. Luo and J. Ma, *Angew. Chem., Int. Ed.*, 2021, **61**, e202112907.

33 J. An, Y. Wang, J. Lu, J. Zhang, Z. Zhang, S. Xu, X. Liu, T. Zhang, M. Gocyla, M. Heggen, R. E. Dunin-Borkowski, P. Fornasiero and F. Wang, *J. Am. Chem. Soc.*, 2018, **140**, 4172–4181.

34 G. Li, C. Foo, X. Yi, W. Chen, P. Zhao, P. Gao, T. Yoskamtorn, Y. Xiao, S. Day, C. C. Tang, G. Hou, A. Zheng and S. C. E. Tsang, *J. Am. Chem. Soc.*, 2021, **143**, 8761–8771.

35 G. Li, T. Yoskamtorn, W. Chen, C. Foo, J. Zheng, C. Tang, S. Day, A. Zheng, M. M. J. Li and S. C. E. Tsang, *Angew. Chem., Int. Ed.*, 2022, **61**, e202204500.

36 G. Li, C. Foo, R. Fan, M. Zheng, Q. Wang, Y. Chu, J. Li, S. Day, P. Steadman, C. Tang, T. W. B. Lo, F. Deng and S. C. E. Tsang, *Science*, 2025, **387**, 388–393.

37 M. Wang, L. Zheng, G. Wang, J. Cui, G. L. Guan, Y.-T. Miao, J.-F. Wu, P. Gao, F. Yang, Y. Ling, X. Luo, Q. Zhang, G. Fu, K. Cheng and Y. Wang, *J. Am. Chem. Soc.*, 2024, **146**, 14528–14538.

38 D. Rivera-Barrera and J. C. Poveda-Jaramillo, *J. Solid State Chem.*, 2021, **294**, 121862.

39 Z. Zhang, J. Wu, Z. Feng, X. Xia, J. Wen, F. Wang, X. Ning, Y. Wen, X. Ke, H. Guan and L. Peng, *J. Phys. Chem. C*, 2024, **129**, 508–517.

40 S. Lu, H. Yang, Z. Zhou, L. Zhong, S. Li, P. Gao and Y. Sun, *Chin. J. Catal.*, 2021, **42**, 2038–2048.

41 R. Zou, C. Shen, K. Sun, X. Ma, Z. Li, M. Li and C.-J. Liu, *J. Energy Chem.*, 2024, **93**, 135–145.

42 C. Zhu, X. Wei, W. Li, Y. Pu, J. Sun, K. Tang, H. Wan, C. Ge, W. Zou and L. Dong, *ACS Sustain. Chem. Eng.*, 2020, **8**, 14397–14406.

43 Y. Fu, L. Zhang, B. Yue, X. Chen and H. He, *J. Phys. Chem. C*, 2018, **122**, 24094–24102.

44 C. Y. Regalado Vera, N. Manavi, Z. Zhou, L.-C. Wang, W. Diao, S. Karakalos, B. Liu, K. J. Stowers, M. Zhou, H. Luo and D. Ding, *Chem. Eng. J.*, 2021, **426**, 131767.

45 L. Liu, F. Cannizzaro, A. Kaychouhi, N. Kosinov and E. J. M. Hensen, *Chem. Eng. J.*, 2024, **494**, 153204.

46 A. R. Richard and M. Fan, *ACS Catal.*, 2017, **7**, 5679–5692.

47 L. Andrews and X. Wang, *Angew. Chem.*, 2004, **116**, 1738–1741.

48 Y. Dong, K. K. Ghuman, R. Popescu, P. N. Duchesne, W. Zhou, J. Y. Y. Loh, F. M. Ali, J. Jia, D. Wang, X. Mu, C. Kübel, L. Wang, L. He, M. Ghoussoub, Q. Wang, T. E. Wood, L. M. Reyes, P. Zhang, N. P. Kherani, C. V. Singh and G. A. Ozin, *Advanced Science*, 2018, **5**, 1700732.

49 E. L. Fornero, A. L. Bonivardi and M. A. Baltanás, *J. Catal.*, 2015, **330**, 302–310.

50 K. Li and J. G. Chen, *ACS Catal.*, 2019, **9**, 7840–7861.

This journal is © The Royal Society of Chemistry 2025

J. Mater. Chem. A, 2025, **13**, 20542–20551 | **20551**